Thin Solid Films 636 (2017) 615–621

Contents lists available at ScienceDirect

Thin Solid Films

journal homepage: www.elsevier.com/locate/tsf

Optical properties of nanocrystalline La_2O_3 dielectric films deposited by radio frequency magnetron sputtering

S.B. Brachetti-Sibaja [a,b], S.E. Rodil [c], M.A. Domínguez-Crespo [a,*], A.M. Torres-Huerta [a], E. Rodríguez [a], A.B. López-Oyama [d]

[a] Instituto Politécnico Nacional, CICATA-Altamira, IPN, Km 14.5 Carretera Tampico-Puerto Industrial Altamira, C.P. 89600 Altamira, Tamaulipas, Mexico
[b] TecNM, Instituto Tecnológico de Cd. Madero, Ave. Primero de Mayo s/n Col. Los Mangos, Cd. Madero, Tam. C.P. 89440, Mexico
[c] Universidad Nacional Autónoma de México, IIM, Circuito Exterior s/n C.U., Coyoacán C.P. 04510, Mexico
[d] Conacyt-Instituto Politécnico Nacional, CICATA, Unidad Altamira Km 14.5 Carr. Tampico-Puerto, Industrial Altamira, Altamira, Tamps. C.P. 89600, Mexico

ARTICLE INFO

Article history:
Received 19 December 2016
Received in revised form 5 July 2017
Accepted 5 July 2017
Available online 6 July 2017

Keywords:
Optical properties
Sputtering
Thin films
Lanthanum oxide
Lanthanum hydroxide
Swanepoel method

ABSTRACT

La_2O_3 thin films were successfully synthesized by r. f. magnetron sputtering technique. The effect of power, deposition time and substrate temperature on the formation and optical properties of the films was investigated. X-ray diffraction (XRD) studies revealed the formation of hexagonal phased La_2O_3 thin films. The influence of sputtering parameters on chemical composition and surface species was studied by X-ray photoelectron spectroscopy (XPS). The optical properties were investigated in the wavelength range of 200–1100 nm. The samples were modelled as a three-phase optical model. Optical constants were calculated at 2 eV from classical dispersion model based on the single Lorentz for dielectric materials.

1. Introduction

Actually, a lot of research efforts is devoted to search for new alternative dielectric materials for complementary metal-oxide-semiconductor (CMOS) devices and materials that increase the optical properties [1–10]. CMOS technology is the basic semiconductor technology for microprocessors, memories and application specific integrated circuits, whereas optical structures are commonly used as non-volatile memory pyro-electric detectors and microwave devices.

Particularly, transparent thin films with good optical properties are demanded in integrated optics. In this relation, lanthanum oxide possesses a lot of properties attractive for industrial and technological applications [11–14]. La_2O_3 films are conventionally prepared using various deposition techniques such as chemical vapor deposition, spray pyrolysis [15–17], electron-beam evaporation, pulsed-laser evaporation and vacuum evaporation [18–20]. Besides, the reactive dc magnetron sputtering method is very promising for the La_2O_3 film fabrication in an amorphous state [21]. A route very few explored to produce this kind of rare earth thin films is the radio frequency (r. f.) magnetron sputtering technique which is one of the most widely used in the manufacture of integrated circuits, resistant materials delaying the corrosion process and optical devices [22–27]. However, the dependence of particle size and optical properties from the synthesis parameters to obtain nanocrystalline lanthanum oxide has not been yet reported. The present study is aimed to find the conditions for the successful deposition of nanocrystalline La_2O_3 thin films on Si (100) substrates by the r. f. magnetron sputtering technique and to assess the differences in the structure, morphology, composition and optical properties depending on deposition parameters.

2. Experimental details

Lanthanum oxide films were deposited on Si (100) substrates using r. f. magnetron sputtering apparatus from a La_2O_3 target (99.99% purity with copper bonding, Plasmaterials) in Ar atmosphere of ultra-high purity. Prior to the La_2O_3 deposition, the Si substrates were cleaned in sonication bath for 20 min with water-isopropyl alcohol-water, thereafter samples were blown with compressed air and dried at room temperature. The base pressure of the sputter chamber was about 2.66 Pa (20 mtorr) with a substrate-target distance of 0.06 m. From previous studies and experience of the team group, it was decided to adjust the r. f. sputtering power at 60 and 90 W; with an Ar flow of 30 sccm. The synthesis was realized at each sputtered power using different times (25, 40 and 60 min) and the substrate temperature adjusted previous to the deposition was 200 °C.

---

* Corresponding author.
E-mail address: mdominguezc@ipn.mx (M.A. Domínguez-Crespo).

http://dx.doi.org/10.1016/j.tsf.2017.07.010

2.1. Chemical, morphological and structural characterization

The chemical composition and band structure of La_2O_3 films were characterized by x-ray photoelectron spectroscopy (XPS) using a VG Microtech Multilab ESCA 2000 system with a CLAM MCD detector, Al K_α (h = 1453.6 eV) radiation, operating at 8×10^{-7} Pa, a pass energy of 20 eV and an energy resolution of 0.1 eV. To obtain the elemental chemical composition, curve fitting of the high resolution XPS spectra were acquired in the regions of the C1s, O1s and La3d photoelectron using the SDP v4.1 software®. Structural features of the as-synthesized La_2O_3 films were analyzed by XRD using a Bruker D8 Advanced, Cu Kα radiation at 35 kV, 25 mA and a scan rate of 0.021 min^{-1}, whereas their morphology was examined by high-resolution field emission scanning electron microscopy (HR FE-SEM), QUANTA™ 3D FEG. The image was acquired using secondary electrons (SE) at 3.0 kV and at room temperature with a work distance of 6.9 mm (50,000×).

2.2. Optical properties

The optical constants and thickness of the films were obtained by spectroscopic ellipsometry (SE). The measurements were carried out by a Jobin Yvon Uvisel DH10 spectroscopic ellipsometer using an incidence angle 70° and a photon-energy range of 1.5–4.5 eV with an interval step of 0.05 eV. The DeltaPsi2 software® was used to fit the experimental spectra with a three-phases optical model: (1) a crystalline Si layer as the substrate; (2) the metal oxide film modeled as one optical layer (OL) and finally (3) a surface layer modeled as an hybrid La_2O_3 OL with variable void percentage.

UV–vis spectra of the as-prepared samples were recorded in the wavelength range from 200 to 1100 nm using a Perkin Elmer double beam spectrometer, the thickness and refractive index were also calculated using Swanepoel method from the interference fringes region.

The waveguide properties of selected sputtered La_2O_3 films were measured with a prism coupler system (model Metricon 2010, Metricon Corporation, Pennington, USA) which comprises three laser wavelengths of $\lambda = 632.8$, 1305 and 1536 nm. The as-prepared lanthanum films were brought into contact with the base of the TiO_2 prism by means of pneumatically operated coupling head, creating a small gap between the film and the prism. Using a mirror, the laser beam was reflected to the base of the prism where it was totally reflected onto a photodetector. The film/prism arrangement was mounted onto a computer-controlled rotation stage to allow the varied angle of incidence. At certain discrete values of the incident angle θ_m, photons can tunnel across the air gap into the La_2O_3 film propagating as a guided optical mode, which causes a sharp drop in the light intensity reaching the detector.

3. Results and discussion

3.1. Chemical composition, structure and morphology

The chemical composition and depth distribution of the constituent elements in the Lanthanum thin films were obtained by XPS. Fig. 1 a–b shows the typical La 3d doublet. The deconvoluted assignments components of the La 3d levels as well as the calculated relative abundances of lanthanum forming the film are also presented in Table 1. The energy difference between the $3d_{5/2}$ and $3d_{3/2}$ peaks is approximately of 16.8 eV suggesting the formation of lanthanum oxide. In all samples, the La 3d core level spectra split the signals in four peaks at 836.71, 841.17, 853.48 and 857.97, eV that correspond to La $3d_{5/2}$ and $3d_{3/2}$ satellite peaks, respectively [28]. To verify the chemical state of lanthanum in the film the binding energy difference BE(O 1s)-BE(La $3d_{5/2}$) was calculated and compared with that reported for reference sample of La_2O_3 [28]. BE difference is commonly employed for chemical bonding characterization due to such difference is a more robust parameter insensitive to BE scale shifts due to dielectric surface charging typical for oxides [29–35]. The O 1s envelopes appeared at a glance as being composed of two main peaks located at ~532.01 eV accompanied with other at ~ 534.45 eV, the first peak (~532 eV) is mainly attributed to La_2O_3 whereas the other peak (~534) could be related with hydroxide and a small quantity of carbonate compounds. The O/La ratio (Table 1) and binding energy differences 532–837 ≅ 305 showed that the La—O binding is mainly formed by La_2O_3, which is in agreement with previous reports [21]. Additionally, it is important to note that lanthanum oxides in hexagonal structure is favored by 0.2 eV/formula unit compare to the cubic, thus we assumed that during deposition process, hexagonal lanthanum initially forms La_2O_3 [36], and then upon exposure to the atmosphere reacts with moisture, leading to extensive surface hydroxylation. It is also clear that sputtered conditions cause a variation in the O/La ratio in the range from 0.67 to 0.77. The chemical environment around the O atoms indicates that, under the synthesis parameters, the films that can be obtained are free of contamination or foreign compounds such as $La_2O_2CO_3$, however, the lanthanum hydroxides or carbonates could be readily formed when the film is exposed to the air [37–38].

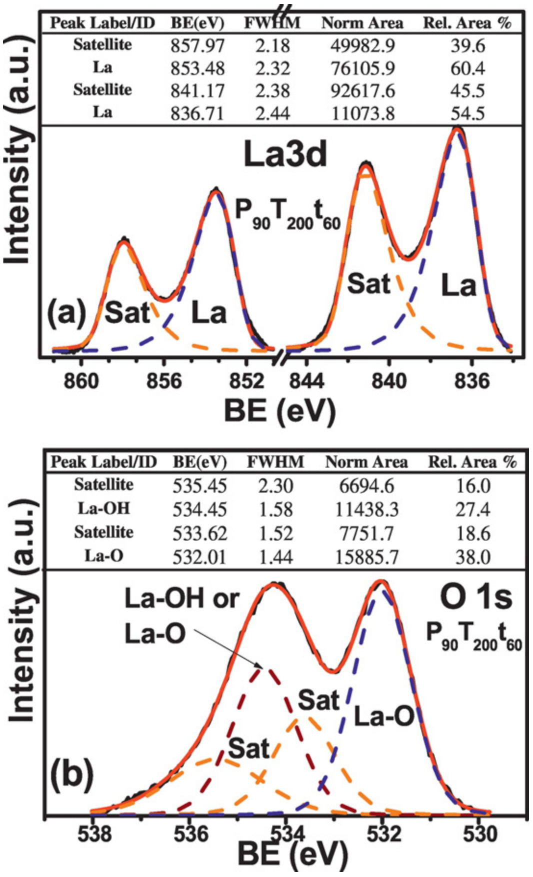

Peak Label/ID	BE(eV)	FWHM	Norm Area	Rel. Area %
Satellite	857.97	2.18	49982.9	39.6
La	853.48	2.32	76105.9	60.4
Satellite	841.17	2.38	92617.6	45.5
La	836.71	2.44	11073.8	54.5

Peak Label/ID	BE(eV)	FWHM	Norm Area	Rel. Area %
Satellite	535.45	2.30	6694.6	16.0
La-OH	534.45	1.58	11438.3	27.4
Satellite	533.62	1.52	7751.7	18.6
La-O	532.01	1.44	15885.7	38.0

Fig. 1. Fitted high resolution photoemission representative spectra of the a) La 3d and b) O 1s regions using different sputtered conditions, with its corresponding magnitude of the multiple splits.

Fig. 2 a-b shows the X-ray diffraction patterns of La_2O_3/Si(100) thin films at increasing r. f. power and deposition time. In general, the peak positions and relative intensities in all XRD patterns match well with the combination of hexagonal La_2O_3 (ICDD 05-0602) [37] $La(OH)_3$ (ICDD 36-1481) [38], and $La_2O_2CO_3$ (ICDD 48-1113) [38]. It is commonly reported for other synthesized methods that lanthanum oxide films are amorphous at low temperatures and eventually crystallized to cubic at 600 °C and hexagonal structures after 750 °C [25]. However, in our case, the hexagonal phase seems to appear when the films are obtained with a substrate temperature of 80 °C and remains at 200 °C. The XRD measurements corroborates that lanthanum oxide films were very reactive in the air with formation of lanthanum hydroxides and

Table 1
Composition in atomic percent of elements identified on sputtered Lanthanum thin films, its corresponding O/La ratio, crystallite size and optical parameters calculate from ellipsometry and UV–vis measurements.

Sample	At. % La 3d	At. % O 1s	O/La ratio	ACS La_2O_3 (nm)	ACS $La_2(OH)_3$ (nm)	ACS $La_2O_2CO_3$ (nm)	Thickness Layer 1 (nm)	Thickness Layer 2 (nm)	Thickness Total (nm)	DR nm s^{-1}
$P_{60}T_{200}t_{25}$	58.8	41.1	0.70	15.2 (1.0)	14.3 (1.1)	15.9 (0.8)	296.7 (9.1)	47.6 (5.5)	344.3	0.229
$P_{60}T_{200}t_{40}$	59.3	40.0	0.67	24.2 (5.1)	44.4 (2.5)	50.4 (5.7)	262.9 (6.6)	88.5 (1.2)	351.4	0.146
$P_{60}T_{200}t_{60}$	56.9	43.2	0.76	13.5 (4.0)	11.2 (0.2)	14.2 (1.2)	312.4 (6.1)	36.3 (3.7)	348.7	0.097
$P_{90}T_{200}t_{25}$	56.9	43.0	0.76	19.3 (1.3)	55.4 (5.4)	69.6 (6.1)	453.1 (9.9)	40.7 (4.6)	493.8	0.329
$P_{90}T_{200}t_{40}$	57.4	42.4	0.74	62.3 (3.5)	63.5(9.6)	43.6 (3.9)	621.7 (10.7)	38.1 (3.3)	659.8	0.275
$P_{90}T_{200}t_{60}$	56.4	43.4	0.77	62.4(2.6)	57.6 (5.6)	54.2 (2.1)	760.4 (19.4)	44.6 (3.8)	805.0	0.224

Sample	Refractive ordinary index (n, at 2 eV)	Refractive extraordinary index (n, at 2 eV)	Ellipsometric measurements			UV–vis measurements	
			Porosity (void) Layer 2	$\omega_{t,E}$	$\omega_{t,o}$	Thickness (nm)	Refractive index (n) at 2 eV
$P_{60}T_{200}t_{25}$	1.744	1.752	17.5 (2.2)	9.2 (0.2)	10.7 (0.4)	–	–
$P_{60}T_{200}t_{40}$	1.761	1.752	11.5 (1.2)	9.2 (0.2)	10.2 (0.2)	–	–
$P_{60}T_{200}t_{60}$	1.738	1.718	15.0 (1.8)	9.9 (0.2)	10.3 (0.4)	301.9	1.558
$P_{90}T_{200}t_{25}$	1.704	1.678	12.4 (1.9)	9.2 (0.02)	10.3 (0.1)	268.9	1.858
$P_{90}T_{200}t_{40}$	1.722	1.706	22 (2.2)	9.6 (0.2)	9.96 (0.1)	273.9	1.776
$P_{90}T_{200}t_{60}$	1.704	1.690	31.3 (3.1)	9.3 (0.2)	10.3 (0.2)	613.7	1.719

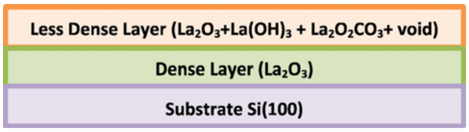

ACS. Average crystallite size. DR, deposition rate.

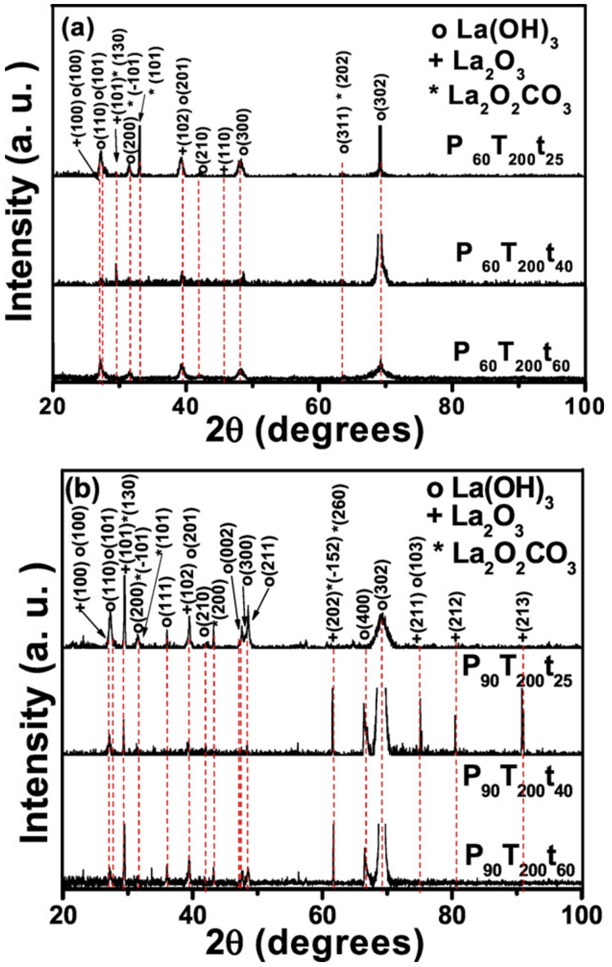

Fig. 2. XRD diffractograms of La_2O_3 films obtained at (a) 60 and (b) 90 W onto Si (100) substrates.

carbonates [26]. Thus, the transformation of h-La_2O_3 to h-$La(OH)_3$ or m-$La_2O_2CO_3$ can be obtained when the La_2O_3 coatings are exposed to the air. The different power, time and substrate temperature cause differences in the intensity and broadening of the peaks; which is correlated with the thickness or particle size of the coating. The deviations are particularly observed at (100), (101), (102), (110), (202), (211), (212), (213) planes for h-La_2O_3; (100), (110), (101), (200), (111), (201), (210), (002), (300), (311), (211), (400), (302), (103) for h-$La(OH)_3$ and (130), (−101), (101), (202), (200), (−152), (260) planes of the monoclinic structure of $La_2O_2CO_3$. The average crystallite size was estimated by the Scherrer's equation $L = 0.9\lambda/\beta\cos\theta$, where λ (0.154 nm) is the wavelength of X-ray-beam, β is the full-width at half maximum (FWHM) and θ is the Bragg angle (Table 1), using the width of the (100) and (102) planes for La_2O_3; (110), (101), (200), (201), (210), (300) and (302) planes for $La(OH)_3$. Additionally, (130) and (−101) planes were used to estimate crystallite size for $La_2O_2CO_3$. It is well known that Scherrer method is a rough estimation due to broadening peaks can be the result of other factors such as microstrains (faulting, dislocations and grain surface relaxation) or even instrumental peak profile among others. Thus, the values showed in Table 1 were obtained from a scheme of deconvolution analysis of each XRD peaks, in order to separate the broadening of each compound, followed by a Gauss fitting. Finally, the crystallite size and uncertainties for the crystallite diameter was calculated using the following equation, which was obtained by propagating the error for λ, β and θ in the Scherrer formula.

$$\frac{\Delta L}{L} = \sqrt{\left(\frac{\Delta\lambda}{\lambda}\right)^2 + \left(\frac{\Delta\beta}{\beta}\right)^2 + (Tan(\theta)\Delta\theta)^2} \qquad (1)$$

The error for the X-ray wavelength was obtained from the diffractometer user manual. The error for both β and θ were obtained from the Gaussian fit to the experimental data. The crystallite size was in the range of 11.2 (0.2) to 69.6 (6.1) nm depending on the deposition conditions. It is obvious that the crystal size in all deposited films is dependent on deposition parameters, i.e. the effect of sputtering power and deposition time on the crystal size was not clear. It was expected that higher power provided energy of the sputtered particles to enhance surface mobility and, consequently, it improves film quality; however, this mobility also causes an alterations of tensile and compressive forces (microstrains; dislocations, vacancies, shear planes) or difference in the incident energy levels resulting in a contracting or broadening of the diffraction peaks.

3.2. Optical properties

Considering an hexagonal structure of the as-prepared La_2O_3 thin films and the rapid transformation in air of h-La_2O_3 to h-$La(OH)_3$ or m-$La_2O_2CO_3$, a light beam passed through the crystal, the beam splits into two rays, with two characteristic an anisotropic model was used to determinate ellipsometric parameters. In anisotropic samples, (ψ, Δ) values vary according to the orientation of the index ellipsoid. In this case, when refractive indices, ordinary (constant) for any direction in the crystal and extraordinary (variable) that depends on the direction. The ellipsometric parameters I_s and I_c measured at $\varphi = 70°$ and its corresponding fitting are shown in Fig. 3a (60 W deposited samples) and Fig. 3b (90 W deposited samples).

However, it should be mentioned that similar results (i.e. the refractive index values and thickness were the same) were also obtained assuming a linear gradient of the refractive index, where the optical layer is modeled as top-bottom refractive indices.

The optical layer was parametrized using a single Lorentz oscillator for dielectric materials model (Eq. (2)), considering anisotropy in the optical properties due to the film composition and the fact that although the films are polycrystalline, they grow with a preferred orientation.

$$\varepsilon = \varepsilon_\infty + \frac{(\varepsilon_s - \varepsilon_\infty)\omega_t^2}{\omega_t^2 - \omega^2 + i\Gamma_0\omega} \qquad (2)$$

where ε is the complex dielectric function, ε_∞ and ε_s are the high-frequency and static dielectric constants, ω_t, is resonant frequency of the oscillator whose energy corresponds to the absorption peak. Γ_0 is the broadening of the oscillator also known as the damping factor and ω is photon energy.

In Fig. 3 a–b, the solid lines represent the simulated values for photon energies from 1.5 to 4.5 eV, while the symbols represent the measured data. In general, the model fits very well, although small discrepancies between the measured and theoretical values can be observed, which are also reflected in a higher figure of merit, as can be observed in Table 1. The ellipsometric measurements clearly support a two-layer structured for the sputtered films. The best fittings were reached using two layer model i.e. a La_2O_3 dense layer followed by a less dense layer composed of $La_2O_3 + La(OH)_3 + La_2O_2CO_3 +$ voids. The thickness of La_2O_3 layer increased with both power and deposition time. However, the dependence of the deposition rate on time at low power (60 W) is very weak. On the other hand, the thickness of the samples deposited at 90 W almost doubled when the deposition time was increased from 25 min to 60 min (Fig. 4). Thick films were obtained at $P_{90}T_{200}t_{60}$ with an interface layer (La_2O_3 dense layer) with a thickness of 760.4 nm combined with a less dense layer ($La_2O_3 + La(OH)_3 + La_2O_2CO_3 +$ voids) of 44.6 nm; whereas for the thinnest films at $P_{60}T_{200}t_{40}$, the best fit was achieved with 296.7 nm for the dense layer, followed with a thickness of 47.6 nm for the outer layer ($La_2O_3 + La(OH)_3 + La_2O_2CO_3 +$ voids). Thus, the La_2O_3/($La(OH)_3 + La_2O_2CO_3$ layer thickness fluctuates from ~344.3 to 805.0 nm and it is mainly affected by power and deposition time.

The refractive index dispersion, *n(E)* of the dense $La_2O_3 + La(OH)_3 + La_2O_2CO_3$ layers fabricated at two different powers values are shown in Fig. 5a–b. In the figure, both ordinary and extraordinary refractive indexed were plotted. Refractive indices around 1.66–1.90 were obtained, in good agreement with values reported in the literature [39].

The polarizability of the films plays a key role for the determination of the size-dependent properties of dielectric materials as well as for the

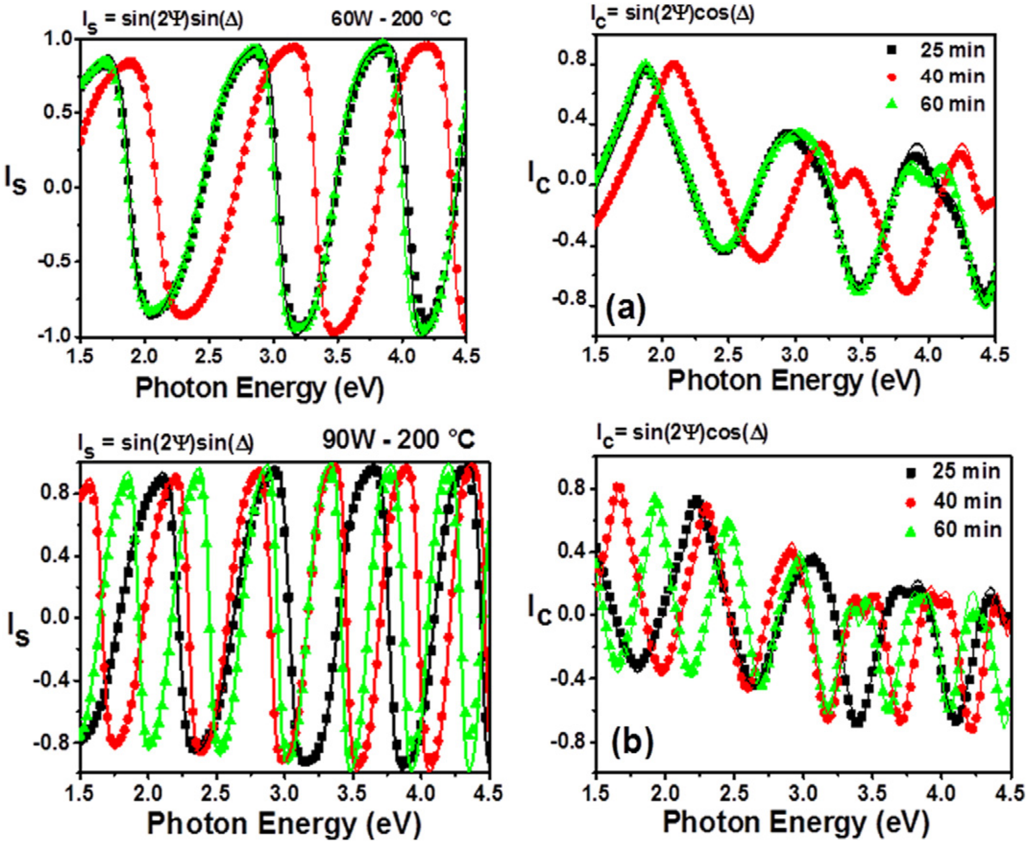

Fig. 3. Optical intensities Is and Ic showing the best fit for sputtered lanthanum oxide films on silicon substrates.

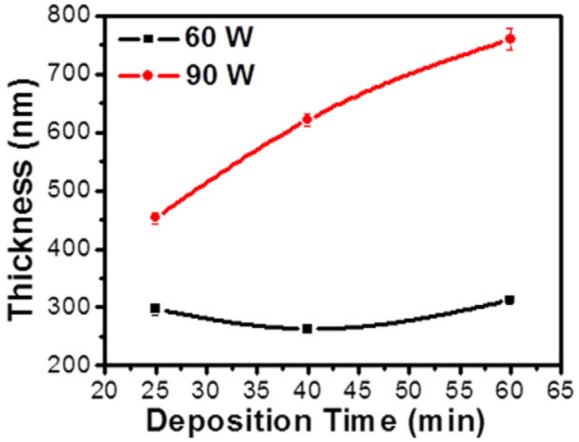

Fig. 4. Dependence of thickness with deposition time of La_2O_3 thin films at 60 and 90 W.

development of new optical components for polarized light with and adequate refractive index. Thus, the variations have been associated with the densification (morphology) and crystallinity of the samples [40].

In order to validate the ellipsometric model and the fitted data, a comparison was realized with UV–vis measurements using as-deposited films on glass substrates (Fig. 6). Two distinct wavelengths regions can be observed in the spectra; at longer wavelengths (>350 nm), transmission exhibits oscillation from interference effects in the transparent films; whereas at shorter wavelengths, (<350 nm), transmission rapidly decreases to zero. The average transmittance of the samples was over 76% in the visible wavelength region. In general, it is notice for the samples that the average transmittance in the near infrared (NIR) spectral range tends to achieve the glass transmittance value (90%). The measured transmittance spectra for samples that displayed interference fringes were used to calculate the optical constants applying the method suggested by Swanepoel [41]. The approach is based on the use of maximal and minimal interference effects in the transparent region of the spectrum for calculation of the refractive index and film thickness [42–45]. The calculated optical properties for UV–vis measurements are shown in Table 1. Accurate values of n and thickness were only considered during calculations whereas other solutions were considered out of the range. Due to the frequency dependence of these parameters at the infrared region, the data were calculated at 2 eV. The results exhibit good agreement between ellipsometric and UV–vis measurements. The refractive index at 2 eV ranged from 1.558 to 1.858 demonstrating a strong dependence on the deposition parameters with thickness varied from 268.9 to 613.7 nm. SEM inset micrographs observed at 50,000×, show a densely packed surface, with small pores, and smooth domes that covers uniformly the surface substrate. Some experimental conditions presented small cracks in the films that tend to disappear with the power and deposition time. The growth process is in agreement with previous works that indicate that the kinetic energy of the expelled particle increases with the power, when the atoms fall on the surface of the substrate are adsorbed and the film is densified. Under these conditions, the lanthanum nanoparticles coalesce and the size gradually increases until a continuous film is formed and the surface becomes irregular. The evolution of the lanthanum film can be explained in terms of the Stranski-Krastanov model, where the growth changes from layers to islands after a monolayer or two due to the change in energy with the successive layer. The small differences in the morphology may explain the discrepancies in the optical parameters.

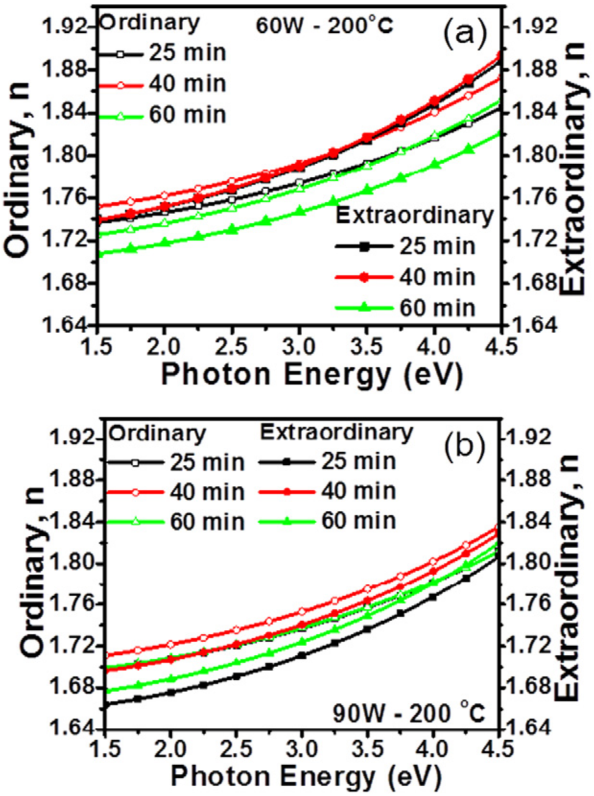

Fig. 5. Ordinary and extraordinary refractive indexes profiles determined by proposed model as function of photon energy.

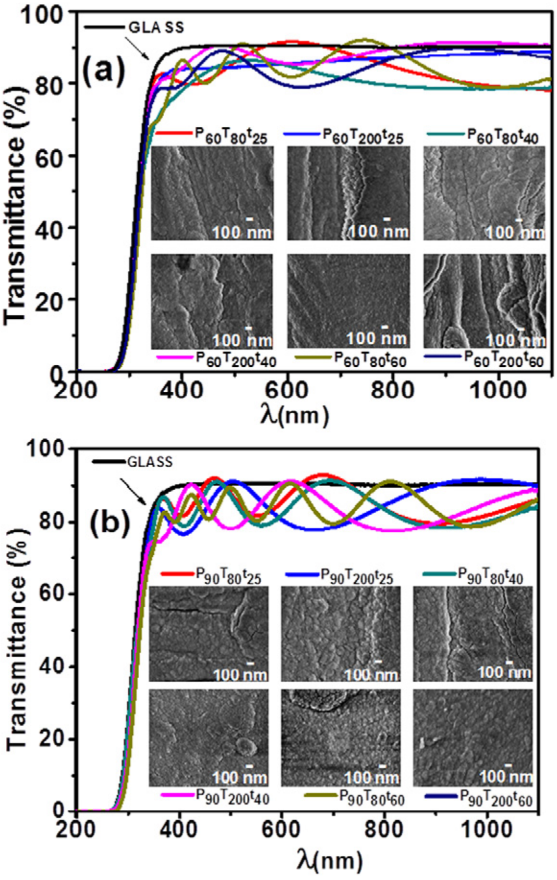

Fig. 6. UV-vis spectra of the as-prepared samples a) 60 W and b) 90 W.

Fig. 7 shows the TE guided modes measured at different wavelengths (633, 1305 and 1536 nm), which propagate in the $La_2O_3 + La(OH)_3 + La_2O_2CO_3$ film synthesized at $P_{90}T_{200}t_{60}$. The sharpness of the intensity drops indicates a good confinement of the light into the film and also the smoothness of the film surface. At shorter wavelength, two TE propagation modes can be clearly identified, enabling

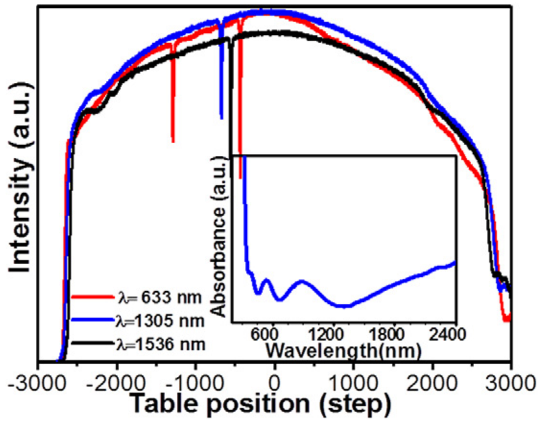

Fig. 7. Propagation modes for La_2O_3 films obtained at $P_{90}T_{200}t_{60}$ and measured with the prism coupling technique at three different wavelengths 633 nm; 1305 nm and 1536 nm and its comparison with UV–vis spectra.

the simultaneous calculation of refractive index and film thickness. For longer wavelengths only one mode propagates along the film. Assuming the thickness calculated at wavelength of 633 nm (636.1 nm), it was possible to obtain the refractive index at 1305 nm (1.957) and 1536 nm (2.011). The values reveal a refractive index that increase as wavelength increases from 1305 to 1536 nm; thus the negative refractive index dispersion (anomalous dispersion) is a consequence of an adsorption band that the material exhibits in this region (see inset in Fig. 7). This behavior is in agreement with the decrease in the film transmittance observed in spectra acquired in the NIR region 1000 to 1500 nm. It is important to highlight that for comparison calculate thickness film by prism coupling (636.1 nm) and Swanepoel method (613.7 nm) are quite similar, however are far from the final average thickness determinate by ellipsometry (805 nm).

Samples obtained at lower power ($P_{60}T_{200}t_{60}$) were also characterized with this optical method. It is worth notice that under these conditions thickness of the film obtained by prism coupling (342 nm) and Swanepoel method (302 nm) well matched with ellipsometric measurements (348 nm); however, there is a discrepancy in the refractive indexes (1.975 at 2.0 eV and 1.558 at 2.0 eV), whereas in the case of ellipsometry the ordinary and extraordinary indexes are about (1.738–1.718 at 2.0 eV). Such discrepancies might be related to inhomogeneity of the film thickness, which became critical when techniques with different spatial resolution are compared.

4. Conclusions

In this work, we report the influence of the synthesis parameters on the optical properties of sputtered La_2O_3 thin films. The XRD results revealed that the crystallite size was in the range of 10–65 nm. The lanthanum films were deposited as La_2O_3 hexagonal structure and when films are exposed to air, the oxide surface film is transform into h-$La(OH)_3$. The XPS analyses corroborate the transformation of h- La_2O_3 to h-$La(OH)_3$ and stoichiometry of the compounds. The application of r. f. magnetron sputtering as a preparation method of La_2O_3 thin films can be used to modulate the optical properties from tailored synthesis parameters. The high refractive index (n ~ 2) and high transmittance in the visible region provide the interesting properties for the lanthanum oxide films as candidate to develop new optical active devices.

References

[1] P. Pisecny, K. Husekova, K. Frohlich, L. Harmatha, J. Soltys, D. Machajdik, J.P. Espinos, M. Jergel, J. Jakabovic, Growth of lanthanum oxide films for application as a gate dielectric in CMOS technology, Mater. Sci. Semicond. Process. 7 (4–6) (2004) 231–236.

[2] S.B. Majumder, M. Jain, R.S. Katiyar, Investigations on the optical properties of sol-gel derived lanthanum doped lead titanate thin films, Thin Solid Films 402 (2002) 90–98.

[3] V.A. Shvets, V.S. Aliev, D.V. Gritsenko, S.S. Shaimeev, E.V. Fedosenko, S.V. Rykhlitski, V.V. Atuchin, V.A. Gritsenko, V.M. Tapilin, H. Wong, Electronic structure and charge transport properties of amorphous Ta_2O_5 films, J. Non-Cryst. Solids 354 (26) (2008) 3025–3033.

[4] J.L. Muñoz-Gamarra, A. Uranga, N. Barniol, Nanomechanical switches based on metal-insulator-metalcapacitors from a standard complementary-metal-oxide semiconductor technology, Appl. Phys. Lett. 104 (2014) (243105-1-5).

[5] H.-S. Kang, M.-J. Lee, W.-Y. Choi, Si avalanche photodetectors fabricated in standard complementary metal-oxide-semiconductor process, Appl. Phys. Lett. 90 (2007) (15118-1-3).

[6] V.V. Atuchin, V.N. Kruchinin, A.V. Kalinkin, V.S. Aliev, S.V. Rykhlitskiĭ, V.A. Shvets, E.V. Spesivtsev, Optical properties of the $HfO_{2-x}N_x$ and $TiO_{2-x}N_x$ films prepared by ion beam sputtering, Opt. Spectrosc. 106 (1) (2009) 72–77.

[7] C.V. Ramana, R.S. Vemuri, V.V. Kaichev, V.A. Kochubey, A.A. Saraev, V.V. Atuchin, X-ray photoelectron spectroscopy depth profiling of La_2O_3/Si thin films deposited by reactive magnetron sputtering, ACS Appl. Mater. Interfaces 3 (2011) 4370–4373.

[8] V.V. Atuchin, V.N. Kruchinin, Y.H. Wong, K.Y. Cheong, Microstructural and optical properties of ZrON/Si thin films, Mater. Lett. 105 (2013) 72–75.

[9] L. Masarotto, L. Frey, M.L. Charles, A. Roule, G. Rodriguez, R. Souil, C. Morales, V. Larrey, Transmission measurements of multilayer interference filters developed for a full integration on complementary metal oxide semiconductor chips, Thin Solid Films 631 (2017) 23–28.

[10] H.W. Wan, K.Y. Lin, C.K. Cheng, Y.K. Su, W.C. Lee, C.H. Hsu, T.W. Pi, J. Kwo, M. Hong. GaAs metal-oxide-semiconductor push with molecular beam epitaxy Y_2O_3 - in comparison with atomic layer deposited Al_2O_3, J. Cryst. Growth, http://dx.doi.org/10.1016/j.jcrysgro.2016.11.118 (in press).

[11] A.H.G. Mekhemer, B.A.A. Balboul, Thermal genesis course and characterization of lanthanum oxide, Colloids Surf. A Physicochem. Eng. Asp. 181 (2001) 19–29.

[12] X. Zhang, A.B. Walters, M.A. Vanmce, NO_x decomposition and reduction by methane over La_2O_3, Appl. Catal. B Environ. 4 (1994) 237–256.

[13] J. Robertson, R.M. Wallace, High-K materials and metal gates for CMOS applications, Mater. Sci. Eng. R 88 (2015) 1–41.

[14] S.Y. Wang, W. Wang, Y.T. Qian, Preparation of La_2O_3 thin films by pulse ultrasonic spray pyrolysis method, Thin Solid Films 372 (2000) 50–53.

[15] J.B. Chen, A.D. Li, Q.Y. Shao, H.Q. Ling, D. Wu, Y. Wang, Y.J. Bao, M. Wang, Z.G. Liu, N.B. Ming, Growth and characteristics of La_2O_3 gate dielectric prepared by low pressure metalorganic chemical vapor deposition, Appl. Surf. Sci. 233 (2004) 91–98.

[16] D.Y. Medina, S. Orozco, I. Hernandez, R.T. Hernandez, C. Falcony, Characterization of europium doped lanthanum oxide films prepared by spray pyrolysis, J. Non-Cryst. Solids 357 (2011) 3740–3743.

[17] M.C. Copel, E. Cartier, F.M. Ross, Formation of a stratified lanthanum silicate dielectric by reaction with Si(001), Appl. Phys. Lett. 78 (2001) 1607–1609.

[18] F.J. Jing, L. Wang, Y.W. Liu, R.K.Y. Fu, X.B. Zhao, R. Shen, N. Huang, P.K. Chu, Hemocompatibility of lanthanum oxide films fabricated by dual plasma deposition, Thin Solid Films 515 (2006) 1219–1222.

[19] A.A. Dakhel, Preparation and optical study of Au nanograins in amorphous La-oxide medium, Colloids Surf. A Physicochem. Eng. Asp. 332 (2009) 9–12.

[20] A.A. Dakhel, Structural and ac electrical properties of oxidised La and La-Mn thin films grown on Si substrates, Mater. Chem. Phys. 102 (2007) 266–270.

[21] V.V. Atuchin, A.V. Kalinkin, V.A. Kochubey, V.N. Kruchinin, Spectroscopic ellipsometry and X-ray photoelectron spectroscopy of La_2O_3 thin films deposited by reactive magnetron sputtering, J. Vac. Sci. Technol. A 29 (2011) (021004-1-5).

[22] G. Bräuer, B. Szyszka, M. Vergöhl, R. Bandorf, Magnetron sputtering–milestones of 30 years, Vac. 84 (2010) 1354–1359.

[23] P.J. Kelly, R.D. Arnell, Magnetron sputtering: a review of recent developments and applications, Vac. 56 (2000) 159–172.

[24] N. Nafarizal, Precise control of metal oxide thin films deposition in magnetron sputtering plasmas for high performance sensing devices fabrication, Proc. Chem. 20 (2016) 93–97.

[25] C. Yang, H. Fan, S. Qiu, Y. Xi, Y. Fu, Microstructure and dielectric properties of La_2O_3 films prepared by ion beam assistant electron-beam evaporation, J. Non-Cryst. Solids 355 (2009) 33–37.

[26] K. Kakushima, K. Tsutsui, S.I. Ohmi, P. Ahmet, V.R. Rao, H. Iwai, Rare earth oxides in microelectronics, Top. Appl. Phys. 106 (2007) 345–365.

[27] C.-C. Hwang, J.-S. Tsai, T.-H. Huang, Combustion synthesis of Ni-Zn ferrite by using glycine and metal nitrates-investigations of precursor homogeneity, product reproducibility, and reaction mechanism, Mater. Chem. Phys. 93 (2–3) (2005) 330–336.

[28] B. Vincent Crist, Handbook of Monochromatic XPS Spectra, The Elements and Native Oxides, Wiley, New York, 2000.

[29] V.V. Atuchin, E.N. Galashov, O.Y. Khyzhun, A.S. Kozhukhov, L.D. Pokrovsky, V.N. Shlegel, Structural and electronic properties of $ZnWO_4$(010) cleaved surface, Cryst. Growth Des. 11 (6) (2011) 2479–2484.

[30] V.V. Atuchin, L.D. Pokrovsky, V.G. Kesler, N.Y. Maklakova, V.I. Voronkova, V.K. Yanovskii, Superstructure formation and X-ray photoemission properties of the $TlTiOPO_4$ surface, Surf. Rev. Lett. 11 (2) (2004) 191–198.

[31] V.V. Atuchin, I.E. Kalabin, V.G. Kesler, N.V. Pervukhina, Nb 3d and O 1s core levels and chemical bonding in niobates, J. Electron Spectrosc. Relat. Phenom. 142 (2005) 129–134.

[32] V.V. Atuchin, V.G. Kesler, N.V. Pervukhina, Z. Zhang, Ti 2p and O 1s core levels and chemical bonding in titanium-bearing oxides, J. Electron Spectrosc. Relat. Phenom. 152 (2006) 18–24.

[33] V.V. Atuchin, O.A. Alekseeva, V.G. Kesler, L.D. Pokrovsky, N.I. Sorokina, V.I. Voronkova, Chemical shifts of atomic core levels and structure of $K_{1-x}Ti_{1-x}$

Sb_xOPO_4, x = 0–0.23, solid solutions, J. Solid State Chem. 179 (8) (2006) 2349–2355.

[34] C.V. Ramana, V.V. Atuchin, V.G. Kesler, V.A. Kochubey, L.D. Pokrovsky, V. Shutthanandan, U. Becker, R.C. Ewing, Growth and surface characterization of sputter-deposited molybdenum oxide thin films, Appl. Surf. Sci. 253 (12) (2007) 5368–5374.

[35] C.V. Ramana, V.V. Atuchin, U. Becker, R.C. Ewing, L.I. Isaenko, O.Y. Khyzhun, A.A. Merkulov, L.D. Pokrovsky, A.K. Sinelnichenko, S.A. Zhurkov, Low-energy Ar^+ ion-beam-induced amorphization and chemical modification of potassium titanyl arsenate (001) crystal surfaces, J. Phys. Chem. C 111 (6) (2007) 2702–2708.

[36] P. Delugas, V. Fiorentini, A. Filippeti, Dielectric properties of rare earths oxides: general trends from theory, in: M. Fanciulli, G. Scarel (Eds.), Rare Earth Oxide Thin Films, Springer-Verlag, Berlin 2007, pp. 225–246.

[37] A.A. Yadav, A.C. Lokhande, J.H. Kim, C.D. Lokhand, Supercapacitive activities of porous La_2O_3 symmetric flexible solid-state device by hydrothermal method, Int. J. Hydrog. Energy 41 (2016) 18311–18319.

[38] X. Li, X. Mao, M. Feng, S. Qi, B. Jiang, L. Zhang, Fabrication of transparent La-doped Y_2O_3 ceramics using different La_2O_3 precursors, J. Eur. Ceram. Soc. 36 (2016) 2549–2553.

[39] W. He, S. Schuetz, R. Solanki, J. Belot, J. McAndrew, Atomic layer deposition of lanthanum oxide films for high-k gate dielectrics, Electrochem. Solid-State Lett. 7 (7) (2004) G131–G133.

[40] L. Armelao, G. Bottaro, L. Bovo, C. Maccato, M. Pascolini, C. Sada, E. Soini, E. Tondello, Luminescent properties of Eu-doped lanthanum oxyfluoride sol–gel thin films, J. Phys. Chem. *C* 113 (32) (2009) 14429–14434.

[41] R. Swanepoel, Determination of surface roughness and optical constants of inhomogeneous amorphous silicon films, J. Phys. E Sci. Instrum. 17 (1984) 896–903.

[42] E. Márquez, J.M. González-Leal, A.M. Bernal-Oliva, R. Jiménez-Garay, T.J. Wagner, Optical properties of amorphous $(As_{0.33}S_{0.67})_{100-x}Te_x$ (x = 0, 1, 5 and 10) chalcogenide thin films, photodoped step-by-step with silver, Non-Cryst. Solids 354 (2008) 503–508.

[43] M. Emam-Ismail, E.R. Shaaban, M. El-Hagary, I. Shaltout, Optical investigation of electron-beam deposited tungst-tellurite $(TeO_2)_{100-x}(WO_3)$ amorphous film, Philos. Mag. B 90 (2010) 3499–3509.

[44] D.Y. Wang, S. Li, H.L.W. Chan, C.L. Choy, Electro-optic characterization of epitaxial $Ba_{0.7}Sr_{0.3}TiO_3$ thin films using prism coupling technique, Curr. Appl. Phys. 11 (2011) S52–S55.

[45] Y. Wang, M. Zhang, X. Zhao, N. Zhao, Optical properties of $Ca_{0.25}Ba_{0.75}Nb_2O_6$ thin films prepared by spinning coating, J. Mater. Sci. Technol. 27 (9) (2011) 821–825.